High-resolution mapping of floodplain topography from space: A case study in the Amazon

Alice César Fassoni-Andrade, Rodrigo Cauduro Dias De Paiva, Conrado de Moraes Rudorff, Claudio Clemente Faria Barbosa, Evlyn Marcia Leão de Moraes Novo

High-resolution mapping of floodplain topography from space: a case study in the Amazon

Alice César Fassoni-Andrade[1,2*], Rodrigo Cauduro Dias de Paiva[1], Conrado M. Rudorff[3], Claudio C. F. Barbosa[4], Evlyn M.L.M. Novo[5]

[1] Institute of Hydraulic Research, Federal University of Rio Grande do Sul (UFRGS), Porto Alegre, RS, Brazil. Caixa Postal 15029. Av. Bento Gonçalves, 9500. CEP: 91501-970.

[2] Institut de Recherche pour le Développement (IRD), Universidade de Brasília (UnB), Brasília, Brazil.

[3] National Center for Monitoring and Early Warning of Natural Disasters, São José dos Campos, São Paulo Brazil.

[4] Image Processing Division, National Institute for Space Research (INPE), São José dos Campos, SP, Brazil.

[5] Remote Sensing Division, National Institute for Space Research (INPE), São José dos Campos, SP, Brazil.

*Corresponding author: Alice Fassoni-Andrade (alice.fassoni@gmail.com)

Graphical abstract:

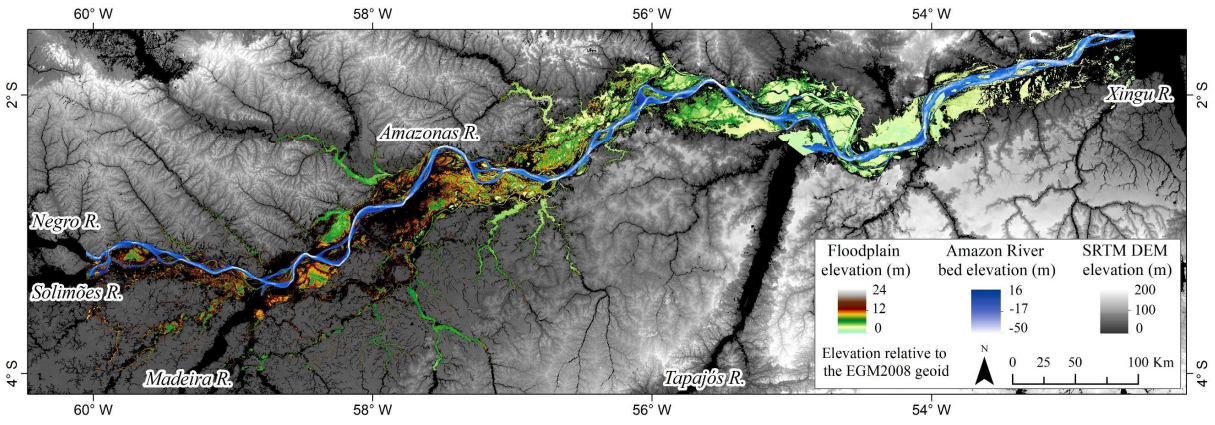

Highlights:

- Landsat flood frequency-based method applied for floodplain topography estimation
- 0.9 m floodplain elevation RMSE after vegetation bias removal with ICESat-2
- River bathymetry (~1100 km extension) obtained from nautical charts; RMSE of 7.5 m
- High-resolution (30 m) water depth and topography maps for middle-lower Amazon
- Storage volume on floodplain open-water areas varies 104.3 km^3 on average each year

Keywords:

Flood frequency; Water level; Topography; Digital Elevation Model; MERIT; SRTM; Amazon; Lakes, Floodplain; Geomorphology changes; Storage volume; Altimetry; ICESat; Landsat; Global Surface Water; Google Earth Engine.

Abstract:

Terrain elevation is essential for land management, navigation, and earth science applications. Remote sensing advancements have led to an increase in the availability of a range of digital elevation models with global to quasi-global land coverage. However, the generation of these models in water bodies requires specialized approaches, such as the delimitation of the shorelines (isobaths) of lakes over time. Therefore, the processing costs are high in complex areas with many lakes. Currently, there is no systematic topographic mapping of lakes and channels in large and complex floodplains using remote sensing data. We present here the first high-resolution topographic mapping (30 m) of the non-forested portion of the middle-lower Amazon floodplain using a new method based on in-situ Amazon river water levels and a flood-frequency map derived from the Landsat Global Surface Water Dataset. Validation using locally derived bathymetry showed a root mean square error (RMSE) of 0.89 m for

floodplain elevation and a good representation of spatial patterns with Pearson's correlation coefficient of 0.77. Our approach for improving topographic representation in open water areas is an alternative to SRTM3 DEM or MERIT DEM, which represents these areas as a flat surface. We also generated the Amazon River bathymetry using nautical charts from the Brazilian Navy (average RMSE of 7.5 m and bias of 5 m), and floodplain depths maps corresponding to the high- and low-water periods of the river flood wave. The results show that the storage volume in the open-water floodplain varies 104.3 km^3 on average each year (from 11.9 km^3 in low-water to 116.2 km^3 in high-water). The method can be applied to any temporarily flooded area to provide the often missing underwater digital topographic data required for hydrological, ecological, and geomorphological studies. The data set developed in this study can be found at https://doi.org/10.17632/vn599y9szb.1.

1. Introduction

Floodplain lakes are important freshwater reservoirs, habitat for aquatic biota, and biogeochemical cycling. In this respect, lake bathymetry is essential information in the quantification of many processes such as water storage (Avisse et al., 2017; Busker et al., 2019; Messager et al., 2016), sedimentation rate, and many other key variables for understanding floodplain morphology and the hydrodynamic interactions between rivers and lakes (Chen et al., 2019; Hamilton et al., 2004; Paiva et al., 2013; Park and Latrubesse, 2017; Trigg et al., 2012). Furthermore, topography is essential for accurate hydrodynamic simulations, since the error associated with topographic data affects, for example, the representation of water flows, flood extent, and storage volume in numerical simulations (Baugh et al., 2013; Paiva et al., 2013; Trigg et al., 2012; Yamazaki et al., 2012).

Digital elevation models (DEMs) can be obtained on global scales, such as the WorldDEMTM (Krieger et al., 2007), Global Digital Elevation Model – ASTER GDEM (Tachikawa et al., 2011), Global Multi-resolution Terrain Elevation Data - GMTED2010 (Danielson and Gesch, 2011), and Shuttle Radar Topography Mission – SRTM (Farr et al., 2007) models. SRTM is the most widely used DEM in hydrodynamic simulations (Paiva et al., 2013; Rudorff et al., 2014a; Trigg et al., 2009; Wilson et al., 2007; Yamazaki et al., 2012). However, these DEMs are affected by vegetation cover or other objects on the surface and are subject to acquisition and processing errors, such as absolute bias, speckle, and stripe noise (Rodríguez et al., 2006). A further limitation is that topographic information below the water surface observed on the date of the satellite overpass cannot be recovered due to specular reflection of the pulse in the opposite direction of the sensor antenna. Although previous studies have developed global or nearly global DEM with correction of the vegetation bias (Loughlin et al., 2016) and other errors (Yamazaki et al., 2017), there is still no database of floodplain topography in regions mapped as open water in the SRTM. In the Amazon

floodplain, for example, lake-floodplain topography has been systematically omitted from hydraulic simulations due to lack of bathymetric information (e.g. Baugh et al., 2013; Wilson et al., 2007; Yamazaki et al., 2012). Performing bathymetric surveys in large wetland systems such as in the Amazon is a difficult task by conventional methods due to its large size and difficulties in accessing remote areas, high cost, and required time for data acquisition and processing. Indeed, few surveys have been performed on floodplain lakes of the Solimões/Amazon rivers (Barbosa et al., 2006; Pinel, 2017; Trigg et al., 2012). Thus, an automated method to characterize lake and channel topography without field surveys has great relevance to improving the representation of water flow in hydrodynamic simulations. Furthermore, such a product could be used for ecological and geomorphological studies.

As an alternative to conventional methods, remote sensing data have been used to estimate lake topography (Arsen et al., 2013; Fassoni-Andrade et al., 2020; Feng et al., 2011; Getirana et al., 2018; Tseng et al., 2016). In these studies, temporal open water surface extent maps from Landsat images and satellite altimetry (e.g. ICESat-1 and 2, Jason-1, 2 and 3, and ENVISAT) were used. Despite these advances, a method that adequately estimates continuous digital terrain elevation over large floodplains with complex topography comprising seasonally variable lakes and intricate networks of channels, such as in the Amazon (D. Alsdorf et al., 2007; Trigg et al., 2012), has yet to be developed. This gap is possibly due to approaches generally considering individual lakes and not well suited to more complex regions with many lakes. The flood frequency-based method described by Fassoni-Andrade et al. (2020) fills this information gap by estimating topography pixel-by-pixel based on a flood frequency map.

This paper presents the first remote sensing-based high-resolution topographic mapping (30 m) of the non-forested portion of a large floodplain system composed of lakes and channels, located in the middle-lower reach of the Amazon River. The method applies the

Fassoni-Andrade et al. (2020) approach by using a time series of water levels for each floodplain pixel, thus characterizing water surface elevation at the pixel level. We also generated bathymetry for the mainstem Amazon River channel based on nautical charts from the Brazilian Navy. Finally, we applied the technique to create depth maps corresponding to the high- and low-water periods of the river flood wave and estimated the average range in water storage for the studied reach.

2. Study area

Topography was estimated in open water regions of the Amazon River floodplain between the confluence of the Negro and the Xingu rivers (-1.59 ºS -60.48 ºW to -3.98 ºS -52.54 ºW; mask in Figure 1). Open water areas correspond to 9% of the Amazon basin wetland areas, a total of 73,458 km^2, and are located mainly in the floodplain associated with the middle-lower Amazon River reach (Hess et al., 2015). The reach from -70.5ºW to -52.5ºW contains about 6,500 lakes (Sippel et al., 1992) that vary in shape, depth, and connectivity degree (Trigg et al., 2012). Along the Amazon mainstem, the variation of open water area in the floodplain increases from the Negro River confluence to the Tapajós River confluence and reduces from that point to the Xingu River confluence (Fassoni-Andrade and Paiva, 2019; Hess et al., 2015; Mertes et al., 1996). The last reach is subject to tidal variation and has few lakes. Therefore, there are more temporally flooded areas in the reach between Parintins and the confluence with the Tapajós River (Figure 1). This reach has large shallow lakes, called depression lakes because they are surrounded by regions of higher overbank deposition of fine sediments (Dunne et al., 1998; Junk et al., 2012; Mertes et al., 1996).

The monomodal pulse of the Amazon River, which varies from 10 to 6 m in amplitude from Jatuarana to Óbidos (Figure 1), strongly influences the variation in the flooded area of this region, which in turn affects numerous ecological processes in the floodplain (Junk et al.,

2011). The floodplain receives nutrients and sediments from the river during the flood period (May/June), while in the low-water period (October/November) the lakes decrease in size or connectivity with the river, changing the local ecological conditions (Junk et al., 1989). For example, the seasonality of algal blooms, tree seed dispersal, and fruits are synchronized with the flooding regime, hence affecting the distributions and feeding habitats of herbivorous and omnivorous fish (Castello et al., 2015; Melack et al., 2009). Furthermore, the growth of aquatic macrophytes in floodplain lakes is related to topography, with a higher concentration occurring towards the littoral zone and a dependence on the lake water level (Junk and Piedade, 1997; Silva et al., 2010).

This study area was chosen because it has a great diversity of lakes and channels of different sizes and shapes reflecting a variety of geomorphological processes, with high variability in the flooded area (Latrubesse and Franzinelli, 2002; Mertes et al., 1996). Additionally, exception for the Lago Grande de Curuai floodplain (Figure 1b), the region has not been well characterized in terms of floodplain hydrodynamics, with many questions still to be answered concerning water flows, the hydrodynamic interaction of the floodplain with the river, and the effects of these processes on the ecosystem (Melack et al., 2009).

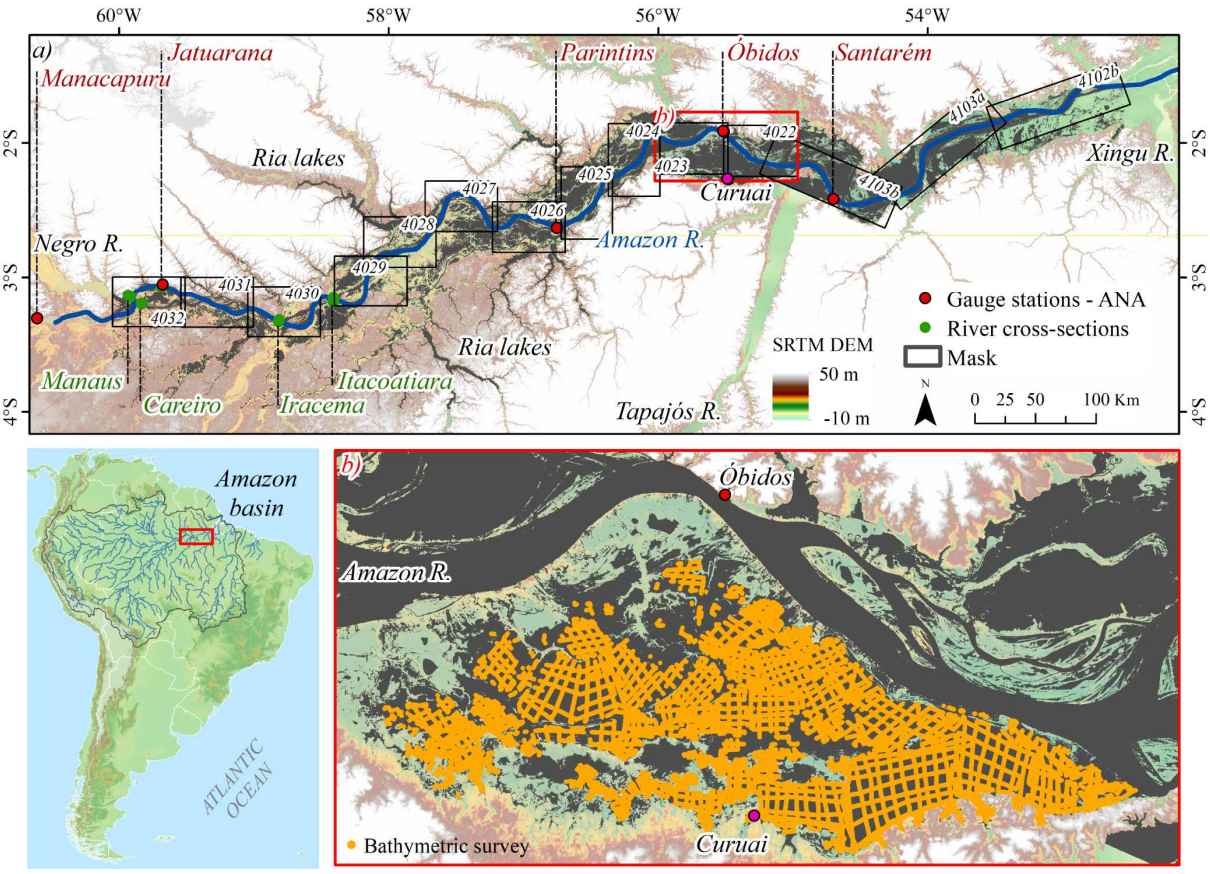

Figure 1. a) Amazon floodplain between the confluence of the Rio Negro and the Xingu River showing the locations of gauge stations and cross-section in the Amazon River and the limits and identifications of nautical charts from the Brazilian Navy. b) Bathymetric survey of the Lago Grande de Curuai floodplain.

3. Data and Methods

The method to estimate the topography in temporally flooded areas is described in Fassoni-Andrade et al. (2020) and depends on a flood frequency map and water level duration curve (obtained from water level time series). In this approach, the bottom level at a pixel is estimated to be the water level whose probability of exceedance is equal to the flood frequency at the same pixel (Box A in Figure 2). Therefore, it is necessary to know the water level duration curve and the flood frequency for each pixel. If only one water level time series is available for the water body, a horizontal surface will be assumed for the whole area, as

assumed in the Flood2Topo application (Fassoni-Andrade et al., 2020). For areas with variable water levels, such as the Amazon floodplain, distributed information on water level is preferable. However, water level time series are not available for all floodplain open water areas. Data from gauging stations in the Amazon River were therefore used to estimate the water level in the floodplain.

The flowchart in Figure 2 shows the processing steps. The open-water mask in the floodplain was firstly defined, followed by interpolation of the water level along the Amazon River, interpolation of the water level in the floodplain, and estimation of the topography. Finally, bathymetric information of the Amazon River from nautical charts of the Brazilian Navy was added in the mapping.

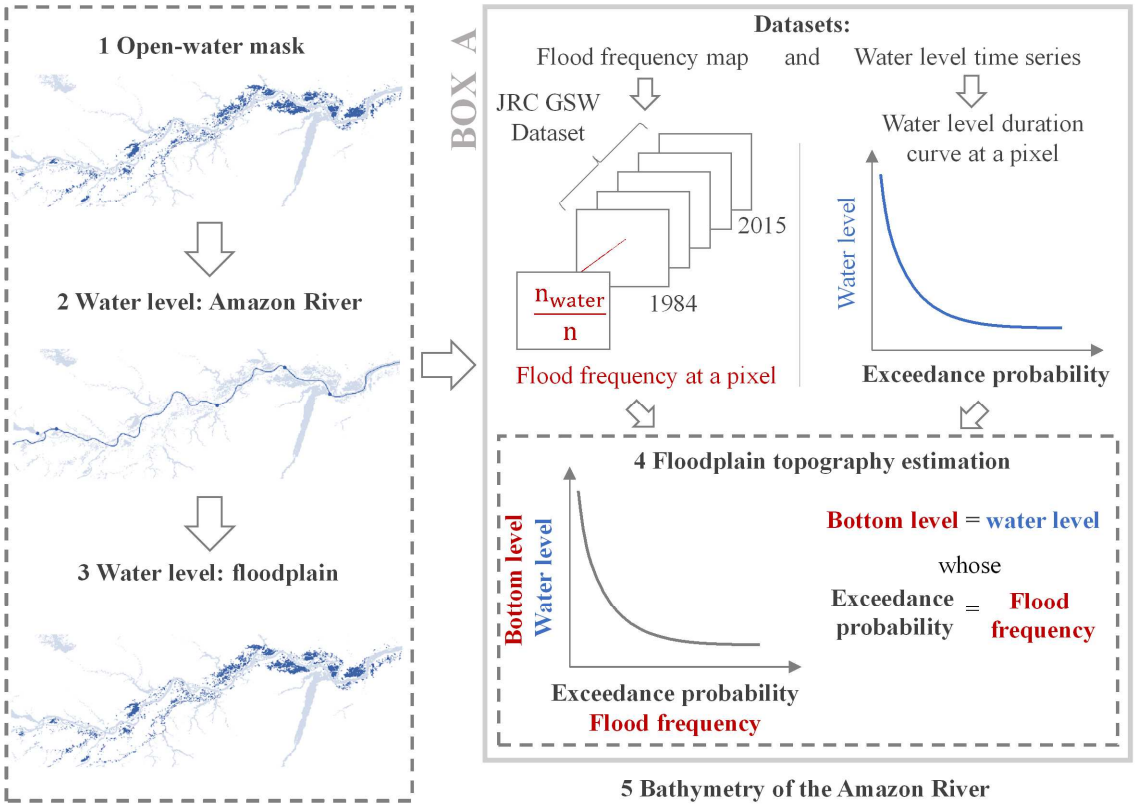

Figure 2. Processing flowchart for topography estimation in the Amazon River floodplain.

3.1. Datasets

A flood frequency map (or open water frequency – OWF map) was used to define open water bodies in the study area. It was calculated from the JRC Global Surface Water (GSW) Monthly Water History v1.0 (Pekel et al., 2016), considering the period from March 1984 to October 2015 (total of 380 months/32 years). This database represents the monthly record of the water presence on a global scale since March 1984, corresponding to the images from the Landsat series classified as water, no-water, and no-data with a spatial resolution of 30 m (Pekel et al., 2016; available at <https://global-surface-water.appspot.com/>). The water cover classification accuracy showed omission errors of less than 5% and commission errors of less than 1% (Pekel et al., 2016). Google Earth Engine (Gorelick et al., 2017) was used to create the OWF map, as described in Fassoni-Andrade et al. (2020; available at https://code.earthengine.google.com/4c07b2c3ee137eb767addca8e005009c). As Landsat sensors are optical, the number of valid observations is limited during the period in which cloud cover is higher, i.e., during the austral summer for the central Amazon basin (Martins et al., 2018), which is the rising period for the Amazon River.

Daily water level data from 1984 to 2015 for five gauge stations in the Amazon River were obtained from the Brazilian National Water Agency (ANA; locations in Figure 1). These data were referenced to the 2008 Earth Gravitational Model geoid (EGM08) according to correction values recommended by Calmant et al. (2012). Data gaps were filled as documented in Text S1 and Figure S1 (Supporting Information). Amazon River bathymetry was obtained by digitizing 14 nautical charts from the Brazilian Navy, which are identified in Figure 1a (available at marinha.mil.br). Bathymetric surveys between Manaus and Óbidos (nautical charts from 4032 to 4022) were carried out between 2010 and 2017, and bathymetric surveys of the nautical charts downstream from Óbidos (4103b, 4103a, 4102b) are older, varying between the years 1997 and 2014.

3.2. Floodplain topography

The open-water mask in the floodplain was defined using the OWF map, i.e., the area delimited by flood frequency greater than 0% during 1984 and 2015. Since this dataset has a spatial resolution of 30 m, numerous floodplain channels and lakes were mapped. Main tributaries (Madeira, Tapajós, and Trombetas rivers) and the Balbina reservoir were excluded since only water level information from the Amazon River was used. The mask is presented by the black region in Figure 1a.

Amazon river's daily water levels (five stations) were interpolated along the river channel. To overcome the channel sinuosity effect on distance calculation between river sections, equidistant points (30 m) were distributed along the channel centerline in the flow direction (blue line in Figure 1a; total length of ~ 1100 km) and used for the linear interpolation procedure. In the reach downstream of Santarém (~349 km in length), the interpolation endpoints were Santarém (distance to the ocean of 768 km; Kosuth et al., 2009) and Ponta do Céu (distance to the ocean of 75 km, Kosuth et al., 2009), which can be referred to as the local average sea level with a water level of 0 m (Kosuth et al., 2009). This reach is subject to maximum tidal wave amplitude variation of 1.5 m at the furthest downstream evaluated point, located 419 km away from the ocean (Kosuth et al., 2009). The linear distribution of the water level along the river channel can be assumed since the cross-validation of the water level at Jatuarana, Parintins, and Óbidos stations showed satisfactory results, as described in the Supporting Information (Text S2 and Figure S2).

As suggested by Alsdorf et al. (2010), local runoff originates only 10% to 20% of the Amazon floodplain water volume. Thus, it is reasonable to assume that the Amazon River water level is sufficient for estimating the floodplain water level. Daily water level time series from 1984 to 2015 at each pixel in the floodplain were estimated by interpolating the water level along the river using the Nearest Neighbor method. Water level duration curves were

then obtained for each pixel by sorting the water level time series data in decreasing order and calculating the exceedance frequency. Finally, the elevation of the lake or channel bottom at a pixel was considered equal to the water level whose exceedance frequency is equal to the flood frequency at the same pixel (Fassoni-Andrade et al., 2020), again relative to the EGM08 geoid.

Daily water level data and the Nearest Neighbor method were chosen for the floodplain topography estimation because this approach showed better results than six exploratory experiments performed and described in the Supporting Information (Text S3 and Table S1). The experiments considered two interpolation methods to estimate the floodplain water level (linear and nearest neighbor) and three time series for calculation of the water level duration curve (daily, monthly, and monthly selected).

3.3. Amazon River bathymetry

The method is not able to estimate bathymetry in permanently flooded regions such as in the Amazon mainstem channel. Therefore, the bathymetry of the river was obtained from the nautical chart information and included in the mapping procedure. According to the Brazilian Navy, values in the Amazon nautical charts used in this study refer to water depths related to the local water surface elevation that remains 90% of the time. This 90% reference level was estimated for each point considering the period from 1984 to 2015. The water surface reference level was then subtracted from the water depth resulting in elevation values (EGM08), and the extracted points were interpolated using the topo to raster method (Hutchinson, 1989) to create an elevation map with 30 m spatial resolution.

3.4. Validation datasets

The estimated water level along the Amazon River and the non-forested portion of the floodplain were validated using ICESat-1 altimetry data derived from the DLAS/ICESat GLA14 Global Land Surface Altimetry Data (Zwally et al., 2014). These data represent the level from 2003 to 2009 of inland water (O'Loughlin et al., 2016) delimited by a static global water mask, and have a height accuracy of 10 cm (Urban et al., 2008). Therefore, some data may represent the emerged lake bottom surface in periods of low-water due to the reduction of the floodplain flooded area (O'Loughlin et al., 2016). The criterion for eliminating outliers resulting from this problem was based on the Amazon River annual flood date. The data were divided according to hydrograph phase in rising (January, February, and March), flood (April, May, and June), falling (July, August, and September), and low-water (October, November, and December), in such a way that the upper (lower) levels greater than the average plus (minus) two standard deviations of each period were eliminated. GLA14 data useful for the evaluation were converted from the EGM96 to the EGM08 datum using the Mensuration Services Program - Geographic Translator (MSP GEOTRANS 3.7, available at earth-info.nga.mil). In addition to altimetry data, water level time series from Vila Curuai Station (Figure 1b) were used to validate the interpolated level in this floodplain, with absolute EGM08 values estimated according to Moreira (2016).

Bathymetric data for the Lago Grande de Curuai were used to validate the estimated topography, which to the authors' knowledge is the only available data for floodplain lakes in the studied region. This dataset was produced by previous studies (Barbosa, 2005; Barbosa et al., 2006; Rudorff et al., 2014a) and corresponds to an extensive bathymetric survey by echo sounder (orange dots in Figure 1b). The SRTM3 DEM v2.1 (Farr et al., 2007) and the Multi-Error-Removed Improved-Terrain DEM (MERIT DEM; Yamazaki et al., 2017) were also compared to the Curuai bathymetry data for open water areas. MERIT DEM improved the SRTM3 DEM by filling some observation gaps over water bodies and removing errors such

as speckle noise, stripe noise, absolute bias, and tree height bias (Yamazaki et al., 2017). However, both models represent open water areas as a flat surface.

In the Amazon mainstem, channel bathymetry was evaluated from river cross-sections surveyed by the Brazilian Geological Survey (CPRM) at Manaus, Careiro, Jatuarana, Iracema, Itacoatiara, and Óbidos gauges (Figure 1).

The following metrics were applied for assessing topography error: mean, standard deviation, minimum, maximum, bias (Equation 1), Pearson correlation coefficient, Root Mean Square Error (RMSE, Equation 2), RMSE of bias-corrected values (RMSE′, Equation 3), and coefficient of determination of bias-corrected values ($R^{2\prime}$, Equation 4)

$$\text{bias} = \frac{1}{n}\sum_{i=1}^{n}\left(x_i^{est} - x_i^{obs}\right) \quad (1)$$

$$\text{RMSE} = \sqrt{\frac{1}{n}\sum_{i=1}^{n}\left(x_i^{est} - x_i^{obs}\right)^2} \quad (2)$$

$$\text{RMSE}' = \sqrt{\frac{1}{n}\sum_{i=1}^{n}\left(\left(x_i^{est} - x_{mean}^{est}\right) - \left(x_i^{obs} - x_{mean}^{obs}\right)\right)^2} \quad (3)$$

$$R^{2\prime} = 1 - \frac{\sum_{i=1}^{n}\left(\left(x_i^{obs} - x_{mean}^{obs}\right) - \left(x_i^{est} - x_{mean}^{est}\right)\right)^2}{\sum_{i=1}^{n}\left(\left(x_i^{obs} - x_{mean}^{obs}\right) - \left(x_i^{obs} - x_{mean}^{obs}\right)_{mean}\right)^2} \quad (4)$$

4. Results and discussion

4.1. Validation of interpolated water levels

4.1.1. Amazon mainstem

Figure 3 shows the differences between interpolated and ICESat-1 daily water levels along the Amazon mainstem. Note that the error does not have a spatial pattern along the river

(bias of 4.24 cm; bias/(maximum-minimum) of 1.32 m; n = 281). RMSE is low (44.85 cm), as it represents less than 5% variation in the amplitude of the Amazon River water surface elevation (~10 m at Jatuarana station).

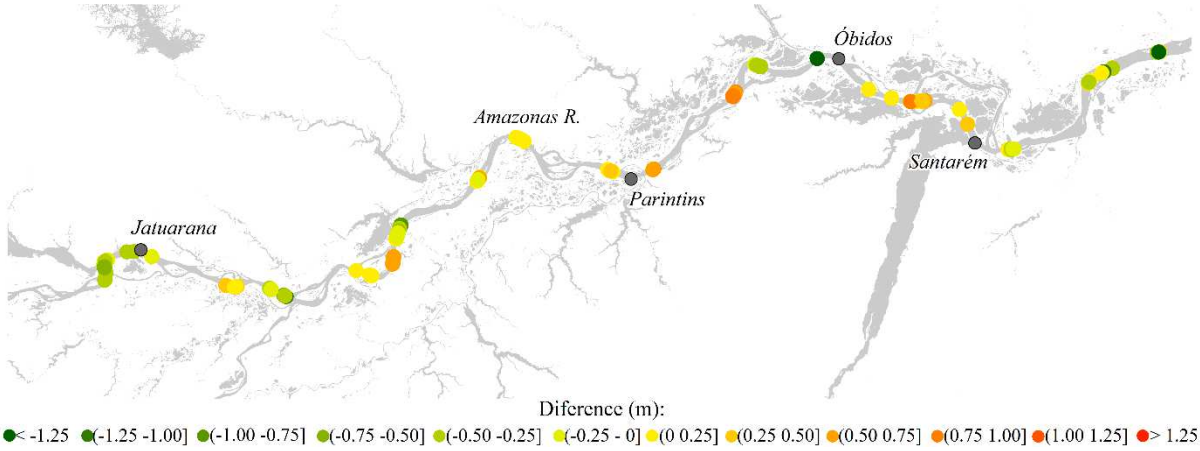

Figure 3. The error of interpolated water level along the Amazon River. Green dots indicate underestimation, red dots overestimation, and yellow dots the smallest obtained errors.

4.1.2. Floodplain

Figure 4 shows the spatial distribution of the errors (interpolated minus ICESat-1 levels) for rising, flood, falling, and low-water periods. The spatial pattern shows that the errors are, in general, random and do not increase with distance from the river. The interpolated water level was overestimated during the rising, flooding, and falling periods and underestimated during the low-water period (bias in Figure 4). The RMSE ranged from 0.65 (falling) to 1.40 (low water), and Pearson's correlation coefficient was high (>0.8). The overestimations are higher in regions farther from the river, such as the points in the black circles of Figure 4. Ria-type lakes that are located in these regions receive important streamflow from the local catchment and the backwater from the Amazon River. Overestimations are higher near Parintins during the rising and high-water periods (points in the red boxes of Figure 4a and b). The falling period has low representativeness since few

data are available and are located in a single region of the floodplain (n = 160; Figure 4c). In the low water period (Figure 4d), the spatial pattern is more random, with some values underestimated by up to -15 m and a higher RMSE (1.40 m). These underestimates may be related to the observations of ICESat-1 inland regions during this period, that is, some of the ICESat footprints may have included land as well as water. Furthermore, with less connectivity among water bodies, water can also be contained in isolated lakes with higher water elevation.

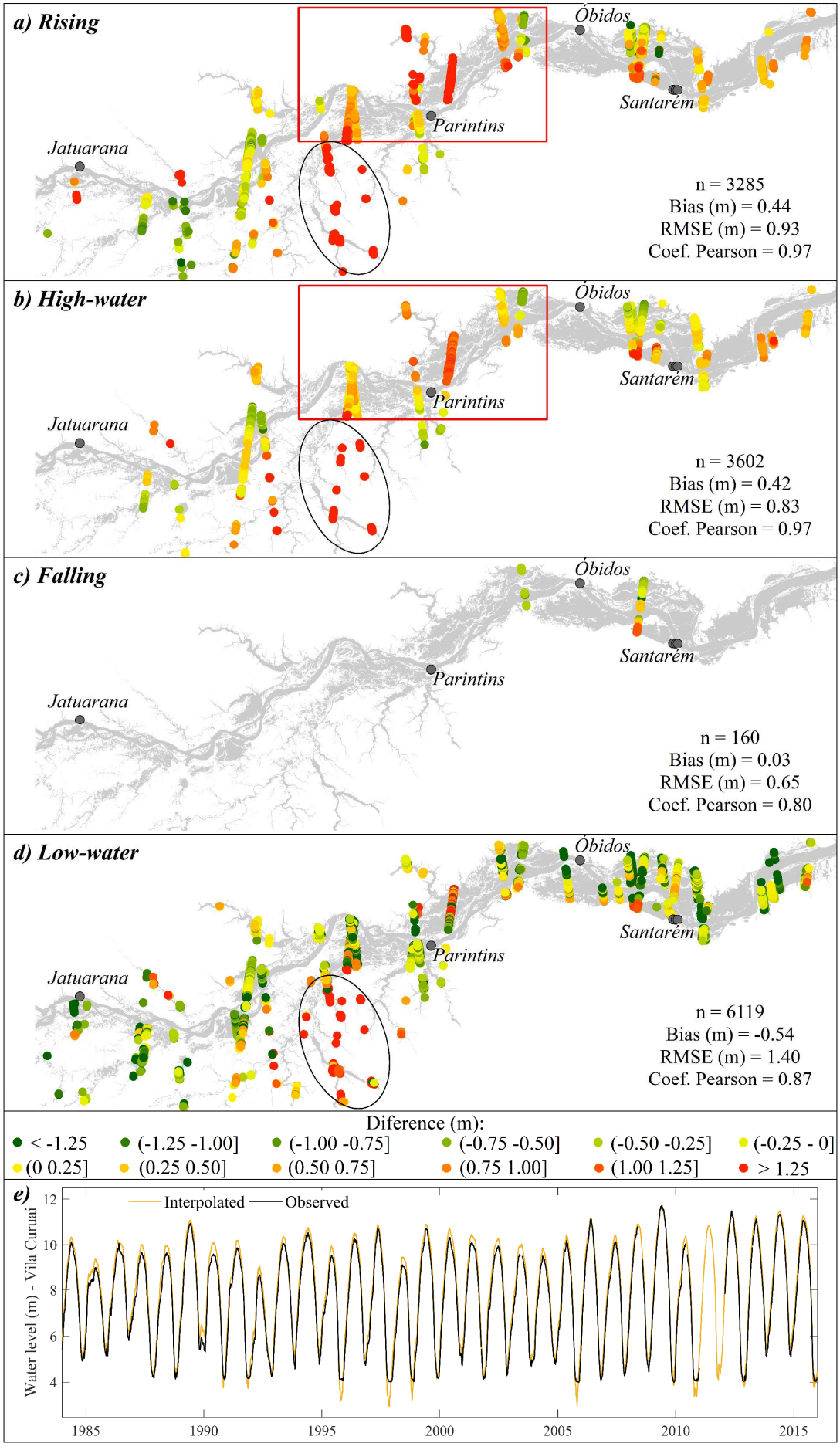
a) Rising
Óbidos
Santarém
Parintins
Jatuarana
n = 3285
Bias (m) = 0.44
RMSE (m) = 0.93
Coef. Pearson = 0.97
b) High-water
Óbidos
Santarém
Parintins
Jatuarana
n = 3602
Bias (m) = 0.42
RMSE (m) = 0.83
Coef. Pearson = 0.97
c) Falling
Óbidos
Santarém
Parintins
Jatuarana
n = 160
Bias (m) = 0.03
RMSE (m) = 0.65
Coef. Pearson = 0.80
d) Low-water
Óbidos
Santarém
Parintins
Jatuarana
n = 6119
Bias (m) = -0.54
RMSE (m) = 1.40
Coef. Pearson = 0.87
Diference (m):
< -1.25
(-1.25 -1.00]
(-1.00 -0.75]
(-0.75 -0.50]
(-0.50 -0.25]
(-0.25 - 0]
(0 0.25]
(0.25 0.50]
(0.50 0.75]
(0.75 1.00]
(1.00 1.25]
> 1.25
e)
Interpolated
Observed
Water level (m) - Vila Curuai
12
10
8
6
4
1985
1990
1995
2000
2005
2010
2015

328

329 Figure 4. The error of the water level in the floodplain estimated by gauge data interpolation
330 for a) rising, b) flood, c) falling, and d) low-water periods. Green dots indicate
331 underestimation, red dots overestimation, and yellow dots the smallest errors; e) Water level
332 at Vila Curuai station.
333
334 Comparison of the interpolated level with the observed level at the Vila Curuai station,
335 located in the Amazon river floodplain, shows RMSE of 0.37 m, bias of 0.33, and Pearson's
336 correlation coefficient of 0.98. Throughout the year, the difference between the interpolated
337 and estimated level is maximal in the high-water period and minimal in the low-water period
338 (Figure 4e). Underestimation of the water level was also observed in some low water periods,
339 as in November 1995, 1998, 1999, 2005, and 2010 (Figure 4e). The loss of connectivity
340 between the gauge station and the main Curuai lake, which remains connected to the Amazon
341 River, may cause this effect. Thus, isolated lakes in the low water period impound water, and
342 the water surface elevation can be higher than that of the river and other lakes. Therefore, the
343 estimation of the water level from the interpolation of the river level is subject to
344 underestimation in floodplain areas that lose connection in the low-water period.
345 The accuracy of the estimated topography is related to uncertainties in the estimation
346 of the floodplain water level. In the approach used here, both floodplain and river water
347 surface elevation are considered to be approximately the same, which is not always true.
348 Alsdorf et al. (2007) and Rudorff et al. (2014b) demonstrated that during the rising and
349 receding limb of the hydrograph differences in water surface elevations between river and
350 floodplain are controlled by the levee topography. During the high water period, widespread
351 overbank flow occurs, and the river-floodplain difference in water surface elevation
352 decreases. Thus, the floodplain water level can be lower than the river water level,
353 overestimating the topography. Moreover, the water can be blocked in some floodplain lakes

during the low-water period, such as in the Lago Grande de Curuai (exemplified in Figure 4e). In this case, the floodplain water level is higher than the river water level, and the topography is underestimated in regions with high flood frequencies (i.e. areas where the level is low).

4.2. Assessment of nautical charts

The Amazon River cross-sections estimated from nautical charts were underestimated with error ranging from 4.3 to 44.5% (average of 20.8%), average RMSE of 7.5 m, and average bias of 5.0 m (Figure 5; Location in Figure 1). The sections are representative of the reach between Manaus and Santarém. The nautical charts for the reach downstream of Santarém are older (nautical charts 4103B, 4103A, 4102B in Figure 1) and have fewer isobaths (lines of equal depth). Therefore, this reach presents greater uncertainty in the river topography relative to the upstream reach.

The comparison of cross-sections in Figure 5 considers the coordinates of the bathymetric surveys from CPRM except for the section at Óbidos. Elevations and cross-section distances from this station were obtained from ANA. Cross-section coordinates were missing and were obtained from those reported in Filizola et al. (2014), which can increase the uncertainty of the estimate. For example, the observed section has high elevation points at the river banks that are not observed in the estimated section (red box in Figure 5). If these points are omitted from the analysis, the error in Óbidos cross-sectional area reduces from 27.8% to 2.6%.

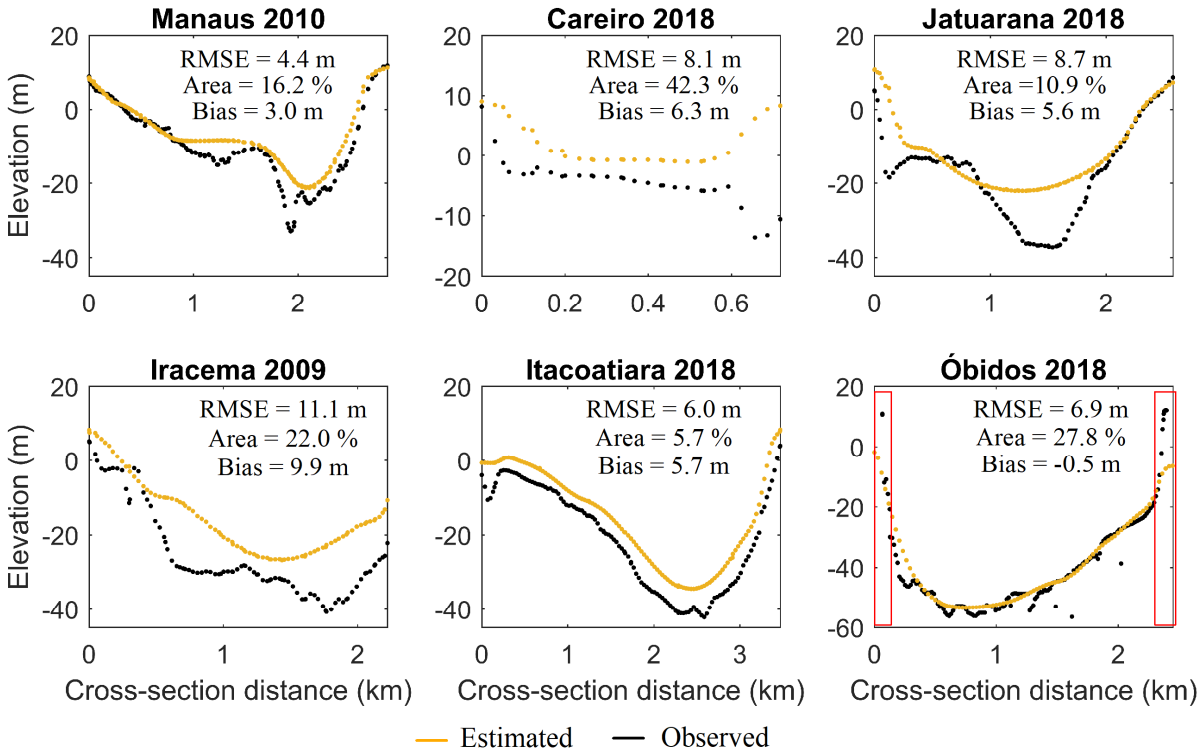

Figure 5. Cross-section transects of the Amazon River (locations shown in Figure 1) estimated from nautical charts and observed at CPRM gauges. Elevation relative to the EGM2008 geoid.

4.3. Validation of topography in Curuai floodplain

4.3.1. Assessment

Figure 6 shows the observed, considering the interpolation of bathymetric survey points (Figure 1 for location), and estimated topography in the non-forested portion of the Lago Grande de Curuai floodplain. In general, there is a spatial-temporal agreement between observed and estimated values. The deepest floodplain channels were overestimated because the method is limited in permanently flooded regions, however, points with flood frequency equal to 100% represent only 1% of the sampled points. Figure 6b and c also exemplify the slatted appearance in the estimated topography due to the Landsat scan line corrector failure (Pekel et al., 2016), carrying these artifacts into the flood frequency and the topographic maps.

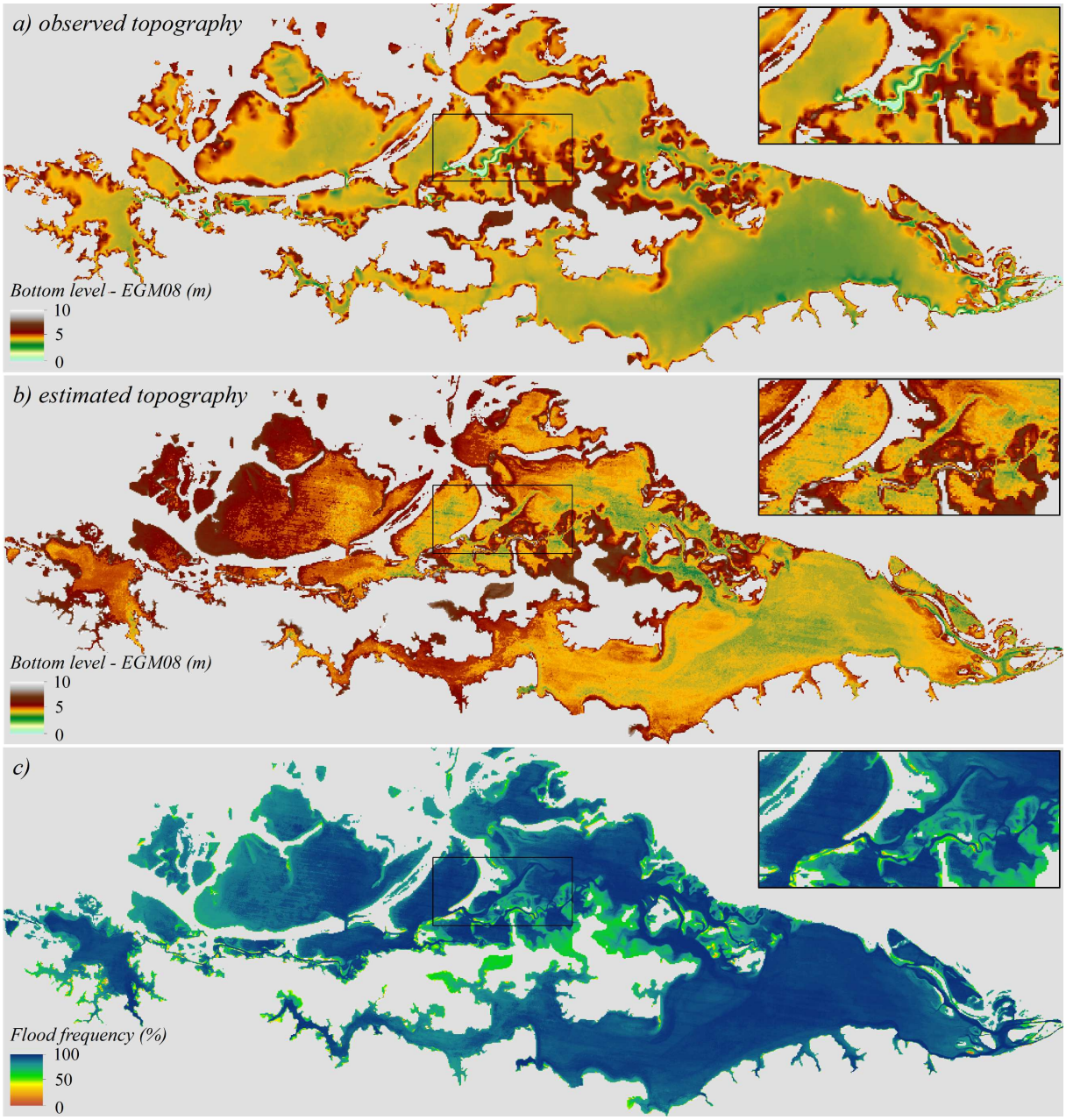

Figure 6. Topography of lakes and channels in the Curuai flood basin derived from (a) interpolation of sonar survey data (Rudorff et al., 2014a) and (b) the flood-frequency processing. c) Landsat Global Surface Water Dataset flood-frequency map

Table 1 presents the metrics of estimated topography considering the approach in this study (non-horizontal water surface, called hereafter Estimated), and by other approaches.

The table also shows the metrics for SRTM3 DEM v2.1 and MERIT DEM in open water areas. Besides, Figure 7 shows the scatterplots of observed versus estimated bottom level by different approaches. The Estimated topography has better metrics than SRTM3 and MERIT. This is especially true for metrics that evaluate the spatial variation of topography, such as Pearson's correlation coefficient, RMSE', and R^{2}' since these models represent the open-water area as a flat surface. Thus, the proposed method is an alternative to estimate the topography in open water areas and replace those areas in global DEMs.

Table 1. Metrics of the observed topography (points in Figure 1) compared to SRTM3 DEM, MERIT DEM, and estimated by different methods

	Mean (m)	**Standard deviation (m)**	**Minimum (m)**	**Maximum (m)**	**Bias (m)**	**RMSE (m)**	**Pearson Coef.**	**RMSE' (m)**	**R^{2}'**
Observed	4.51	1.39	-11.66	9.54	-	-		-	
SRTM3 DEM	1.31	1.03	-5.00	28.00	-3.20	3.55	0.22	1.53	0
MERIT DEM	4.72	1.64	-1.01	27.78	0.21	1.40	0.59	1.38	0
Tseng's approach	4.44	1.38	3.14	12.10	-0.06	1.21	0.62	1.21	0.24
Fassoni-Andrade's	5.45	1.40	3.14	11.90	0.94	1.47	0.67	1.13	0.34
Estimated	**5.30**	**1.45**	**2.75**	**12.49**	**0.79**	**1.30**	**0.73**	**1.04**	**0.44**
Estimated bias-corrected	**4.51**	**1.02**	**2.39**	**9.17**	**0.00**	**0.89**	**0.77**	**0.89**	**0.59**

The methods proposed by Tseng et al. (2017) and by Fassoni-Andrade et al. (2020) were also applied to estimate the topography (called hereafter Tseng's and Fassoni-Andrade's approaches; Table 1). In Tseng's approach, the maximum and minimum water level at Óbidos station, located in the Amazon River near Curuai floodplain, were used so that the topography was obtained pixel-by-pixel by multiplying the probability of no-flood by the water level amplitude and adding the minimum level (Tseng et al., 2017). Thus, this method assumes a linear water level duration curve, as exemplified in Figure 7f, which also shows the observed

water level duration curve in Óbidos. Analysis of these curves shows that Tseng's approach underestimates the bottom level in regions of flood frequency between 20 and 100% and overestimates in regions of flood frequency between 0 and 20%. As this approach underestimates topography, overestimation errors are compensated, resulting in a lower bias and RMSE and closer mean and standard deviation to the observation reference compared to the Estimated topography (Table 1). The vegetation bias is an example of overestimation error and is discussed in section 4.3.2. In contrast, measures of the topography variation of Tseng's approach (Pearson, R^2' and RMSE') are inferior (also in Figure 7c) than approaches using the observed water level duration curve.

Fassoni-Andrade's approach is the same as this study but considering a single water level time series, i.e., the authors assumed a flat-water surface without distributed level information on the floodplain. The water level duration curve at Óbidos station used in Fassoni-Andrade's approach resulted in higher bias and RMSE compared with Estimated topography and Tseng's approach. In contrast, it showed a better representation of topographic variation than Tseng's approach (Pearson, R^2' and RMSE'; Figure 7d). In conclusion, the Estimated topography in the present study provided results that are better than those assuming a linear water level duration curve (Tseng's approach) and non-distributed water level in the floodplain (Fassoni-Andrade's and Tseng's approaches).

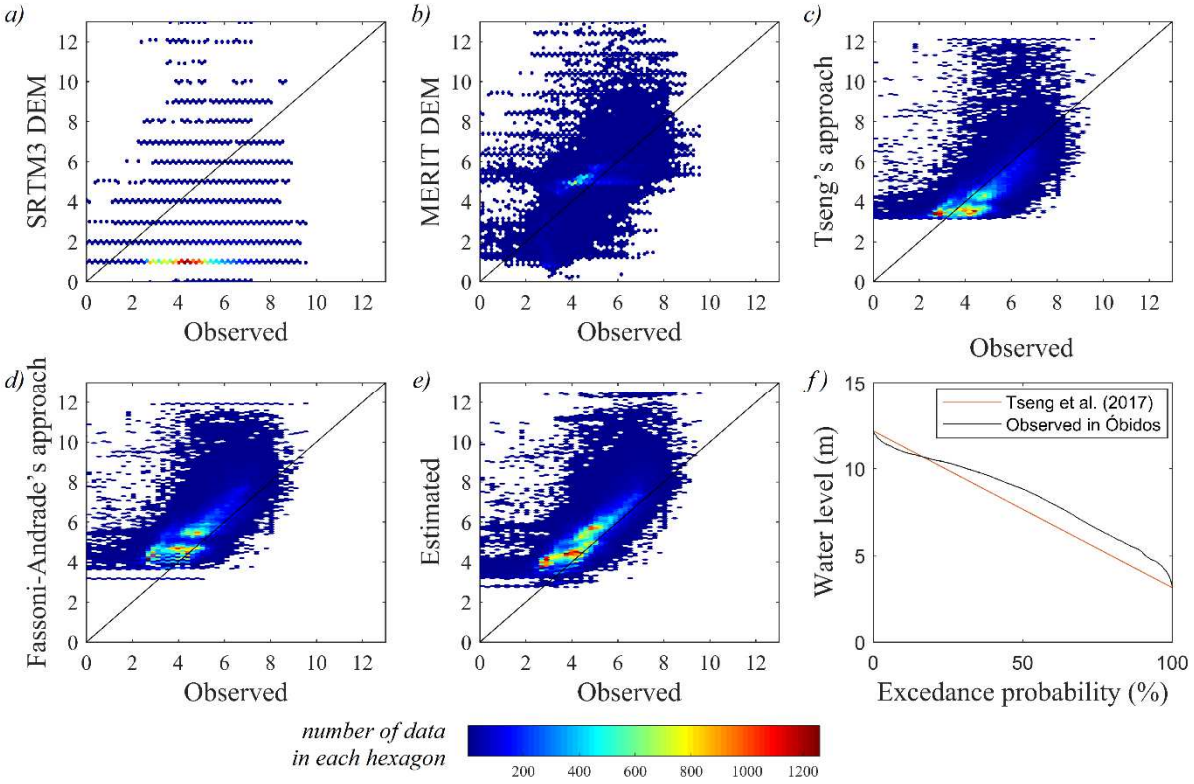

Figure 7. Scatterplots of observed versus estimated bottom level in Curuai floodplain. Note the higher (lower) density of spots in red (blue). a) SRTM3 DEM b) MERIT DEM; c) Tseng's approach; d) Fassoni-Andrade's approach; e) Estimated topography; f) Water level duration curve estimated by Tseng's approach, and observed in Óbidos.

4.3.2. Bias correction

The topography mapping is subject to two main sources of uncertainty: the estimation of water elevation based on linear interpolation of stream gauge data (Section 4.1), and the flood frequency mapping based on the GSW Monthly Water History. In addition to having errors associated with the Landsat data (e.g. cloud cover and scan line corrector failure), the classification of water- covered surfaces in this data set does not consider the inundated vegetation areas where the vegetation height is greater than the water surface elevation. Since these areas are classified as flooded only when the water level is equal to or greater than the vegetation height, the flood frequency map represents the flood above the vegetation, and

454 therefore the estimated topography has a bias related to vegetation. Furthermore, since the
455 mapping has 30 m spatial resolution and a 30-year period is considered, the misclassification
456 in the images is also related to the spectral mixture of reflectance from flooded surfaces and
457 temporal changes in the surface.

458 The floodplain is vegetated by alluvial forest, shrubs, and seasonally variable
459 macrophytes that include emergent grass species (e.g., Hymenachne amplexicaulis, Oryza
460 perennis, and Paspalum repens) and free-floating assemblages (e.g., Eichhornia crassipes,
461 Ludwigia spp., Neptunia oleracea, and Pistia stratiotes) (Silva et al., 2013). The height of
462 these vegetations can be complex to characterize due to water level variation, vegetation
463 types, and phenology. For example, aquatic macrophytes, predominant in floodplain lakes,
464 have a growth pattern that follows water level variation. This vegetation establishes in the
465 terrestrial phase and only its top is not submerged in the aquatic phase until its decline (Junk
466 and Piedade, 1997; Piedade, 1993). Thus, the height of this floating vegetation is related to
467 permanence in the environment and the water level variation. At the same time, the landscape
468 can be composed of higher vegetations that lose their leaves during flooding and/or lower
469 vegetations with high greenness, increasing the spectral mixture from flooded surfaces.
470 Therefore, the mosaic of different vegetation heights, adaptations to flood, and variation in
471 water level induce complex bias in the flood frequency map.

472 To illustrate the vegetation bias, the terrain elevation error was related to the
473 vegetation type in the middle-lower Amazon (Figure 8). The error was calculated from the
474 terrain elevation Estimated and observed by the ICESat-2 altimeter (launched in September
475 2018; available at openaltimetry.org). ICESat-2 data were selected between September 2018
476 and November 2019 considering the following criteria: 1) data collected in the low-water
477 period (October to December); 2) no-water; 3) cloud-free condition; 4) data uncertainty
478 smaller than 0.5 m. Vegetation cover was obtained for the ICESat-2 points considering the

1996 high-water and 1995 low-water mappings elaborated by Hess et al. (2015). Figure 8 shows the terrain topographic error (Estimated minus ICESat-2 data) for 12 classes considering the vegetation variation in the dual-season (Hess et al., 2015). The mean error (black dots) and variation of the error (color bar) increase with increasing of the vegetation height (Herbaceous/bare; Shrub; Forest). Regions with high amplitude of water level (color bar in blue) have greater error than regions with a small amplitude (color bar in orange) since the higher water level can exceed the higher vegetation. Besides, error variation possibly increases from herbaceous to the forest because changes in the dossel structure increase height variability.

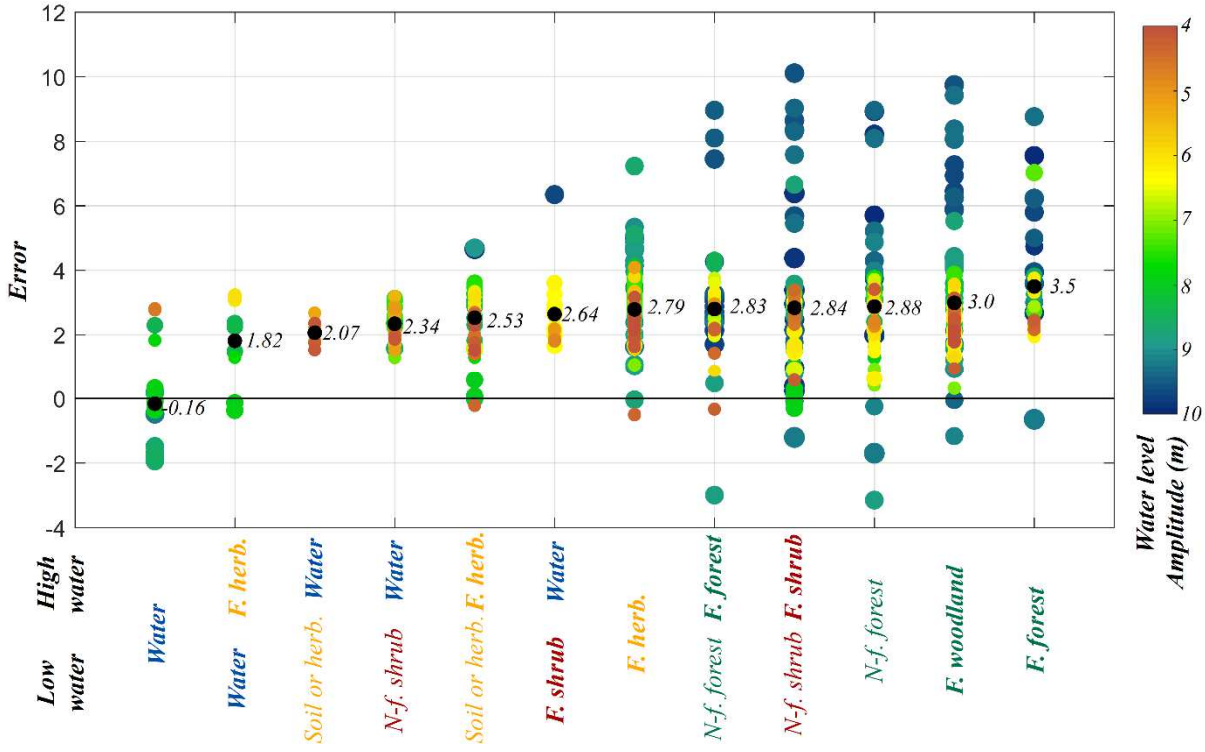

Figure 8. Bottom level error (Estimated minus observed from ICESat-2) and vegetation cover in the middle-lower Amazon study area: Open water (Water); Aquatic macrophyte (flooded herbaceous; F. herb.); Non-flooded bare soil or herbaceous (Soil or herb.); Non-flooded or Flooded shrub (N-f. or F. shrub); Flooded woodland (F. woodland); Non-flooded or Flooded forest (N-f. or F. forest).

Bias correction of the topographic map can be done in a simple approach by relating the flood frequency with the error. Figure 9b shows the relationship between flood frequency and the error in the Estimated topography of the Lago Grande de Curuai. As the flood frequency decreases, topography overestimation increases, i.e. larger errors occur in regions of lower flood frequency. Thus, a linear relationship between flood frequency and ICESat-2 error (Figure 9a and Equation 1) was adjusted to reduce vegetation bias in the middle-lower Amazon. Figure 9c shows the relationship between flood frequency and the Estimated topography error in the Lago Grande de Curuai after bias correction. Note that bottom level bias reduced to zero, RMSE reduced from 1.30 m to 0.89 m, and Pearson's correlation coefficient increased from 0.73 to 0.77 in this floodplain (Table 1; Estimated bias-corrected).

$$\text{Bottom level corrected} = \text{Bottom level} - (3.3619 - 0.0301 \cdot FF) \quad (4)$$

Where the bottom level is in meters and the flood frequency (FF) is in $\%$.

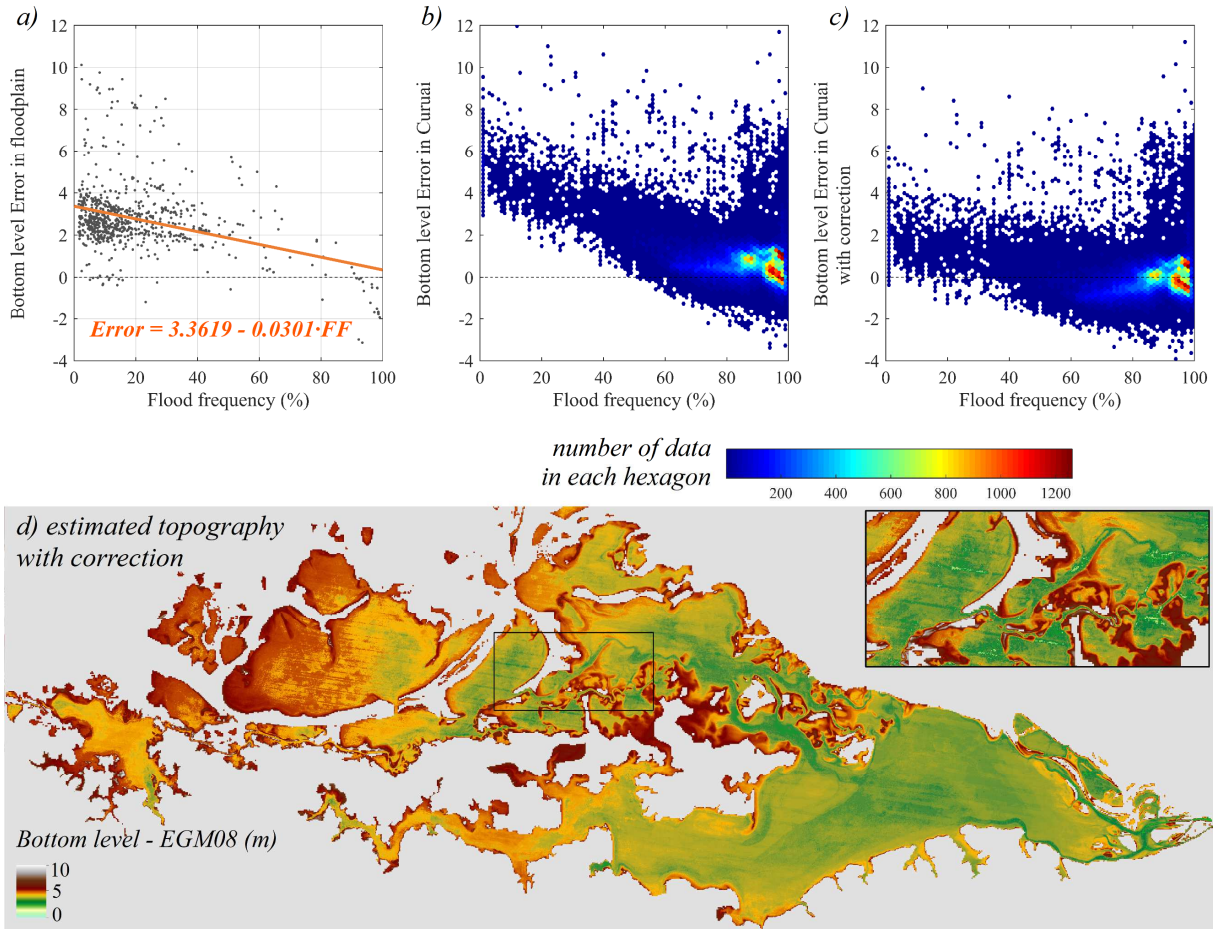

Figure 9. a) Linear fit of the bottom level error (Estimated minus observed from ICESat-2) and the flood frequency in the middle-lower Amazon study area; b) Flood frequency versus bottom level error before and c) after bias correction; d) Estimated topography with bias removal in the Lago Grande de Curuai.

5. Middle-lower Amazon floodplain topography and water depth maps

The estimated topographic mapping of lakes and channels in the non-forested portion of the Amazon floodplain, as well as the Amazon River bathymetry, is presented in Figure 10 and for a region in the Amazon floodplain in Figure 11. MERIT DEM does not represent the topographic variation in water bodies (Figure 11a). In contrast, the estimated topography represents many topographic details, such as the complex network of interconnected channels (Figure 11b). Therefore, the proposed method is promising for estimating topography in

temporarily flooded areas. Also, the estimated floodplain topography is representative of the period from 1984 to 2015, thus, geomorphological changes in the fluvial channel and the floodplain during that period were considered. The application of the method considering different periods is a potential impactful application to assess geomorphology changes in a dynamic environment.

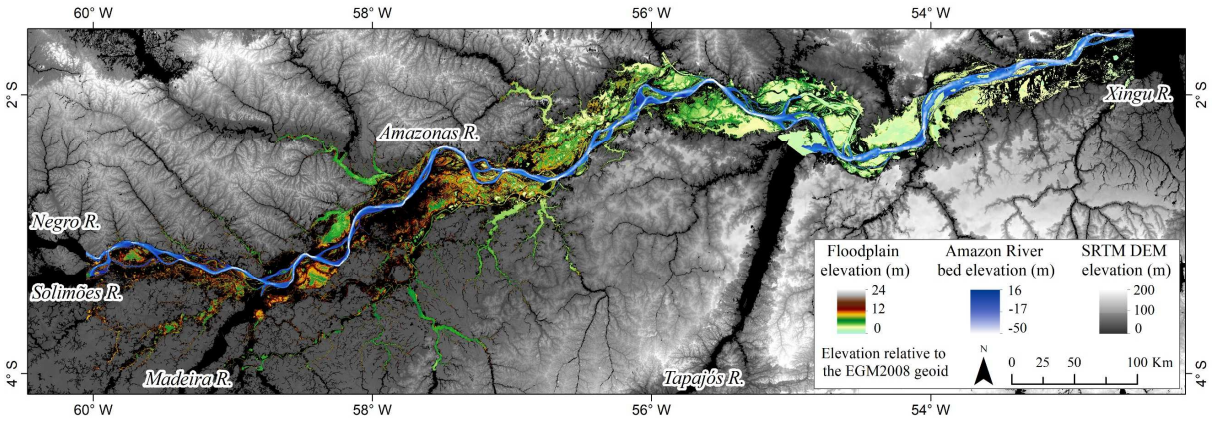

Figure 10. Estimated topography mapping of lakes and channels in the Amazon floodplain and Amazon River bed elevation.

The flood frequency-based method does not estimate topographic information in permanently flooded regions; therefore, all regions in the topography mapping that have flood frequency equal to or close to 100% are represented by the lowest water level observed in the period (1984 to 2015), as shown in Figure 11c. This occurs, for example, in ria-type lakes (exemplified in Figure 1). These lakes with dendritic shapes are deeper, have flood frequency close to 100% (Junk et al., 2012; Latrubesse, 2012), and receive water from both the local basin and the main river (Ji et al., 2019; Lesack and Melack, 1995). The flood frequency map provided in the data set can be used to evaluate permanently flooded areas where the topographic map is inaccurate.

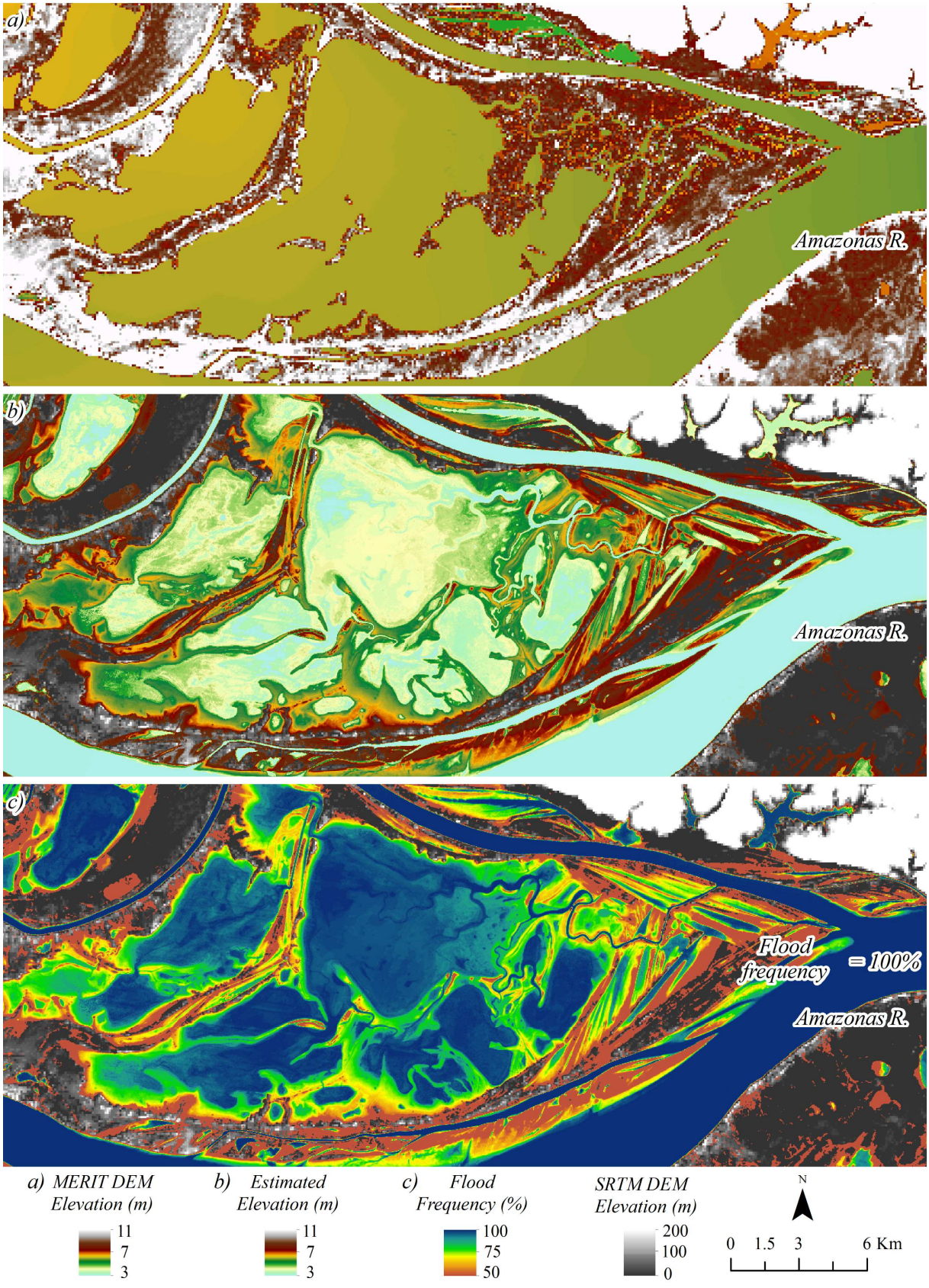

Figure 11. a) MERIT DEM elevation with flat water surface; b) Estimated topography and c) Flood frequency in an Amazon floodplain. Elevation relative to the EGM2008 geoid.

548

549 Water depth maps in the floodplain open-water areas for the high-water and low-water
550 periods were created considering the maximum and minimum levels corresponding to the
551 average annual level between 1984 and 2015 calculated for each pixel (Figure 12a, b, and c).
552 For example, these reference levels in Jatuarana and Óbidos are, respectively, 20.6 and 10.9 m
553 for high-water, and 10.6 and 4.9 for low-water (Figure 12a). The cumulative water depth
554 frequency in the floodplain (shown in Figure 12d) can be used to estimate the percentage of
555 the area with a depth less than or equal to a reference depth. For example, 75% of the open-
556 water area during the low-water period (total area of 8,159 km^2) has a depth of less than or
557 equal to 2 m. In contrast, 75% of the open-water area has a depth of less than or equal to 8 m
558 in the high-water period (total area of 19,177 km^2). Figure 12e shows the active storage
559 volume in the open-water floodplain for both periods.

560 The maximum depth in temporarily flooded areas (Flood frequency <100%) is given
561 by the range of water level variation over the considered period (i.e., the range from
562 maximum to minimum water level). In the case of the Amazonian floodplain lakes that are
563 subjected mainly to the monomodal Amazon River flood pulse, the method assumes that the
564 variation of the lake water level amplitude is equal to the river amplitude. In other words, the
565 maximum water depth in temporarily flooded areas is always smaller than the water level
566 amplitude of the Amazon River. As the river water level amplitude decreases from upstream
567 to downstream (Figure 12a), the lake depth also decreases, therefore, upstream lakes are
568 deeper than downstream lakes (Figure 12b e c). Trigg et al. (2012) also observed a
569 relationship between the Solimões River water level amplitude and the depths of floodplain
570 channels subject only to the river flood wave. The authors showed that the average depth of
571 these channels, obtained by field survey during the high-water period (2009), has values close
572 to the river average amplitude. Results also agree with Alsdorf et al. (2010), who indicated

573 that the water depths follow an upstream-to-downstream trend in the Amazon floodplain
574 using gravimetric and imaging satellite methods.
575

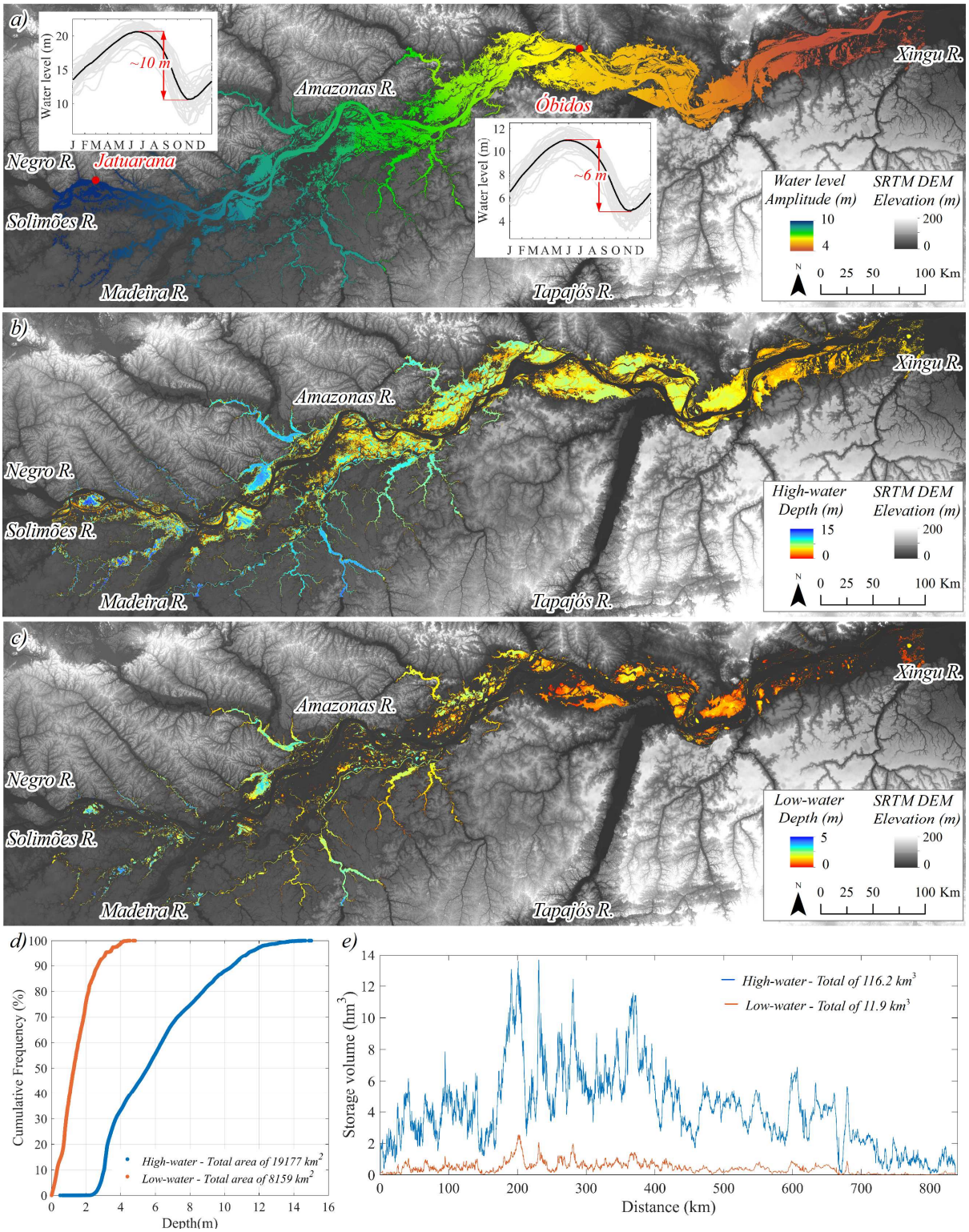

576

Figure 12. a) Amplitude of the water level; Water depths maps for the period of b) high-water and c) low-water; d) Cumulative frequency of water depth in the floodplain open-water areas; e) Storage volume in the open-water floodplain.

Average active volume on the floodplain, i.e., the amount of water varying in the high-water and low-water periods, represents a total of 104.3 km^3 each year (the range from 11.9 km^3 to 116.2 km^3). The topography is not estimated in the whole flooded vegetation area, so this is an underestimated value, but it represents a considerable volume. Frappart et al. (2019) showed that storage variation in this region of the Amazon basin has a more significant contribution of surface water than soil moisture and groundwater (>50%). Alsdorf et al. (2010) found storage amplitude of Amazon floodplain values of 50 km^3 and 60 km^3 for two square regions (330 km x 330 km) located near Óbidos and Manaus, respectively. Although the range of areas is different, our estimate seems reasonable, representing 95% of the total estimated by Alsdorf which included all flooded vegetation areas. In the Curuai floodplain (Figure 6 for location), the storage amplitude was 8.4 km^3, which is slightly more than the 7.9 km^3 estimate by Rudorff et al. (2014b).

6. Summary and conclusions

We presented the first high-resolution topographic mapping (30 m) of lakes and channels of the middle-lower Amazon floodplain using a method based on flood-frequency mapping derived from Landsat images. The seasonally flooded area mapped (47 thousand km^2) represents topographic variations between 1984 and 2015 and corresponds to 54% of the wetland area of this reach. We also created a bathymetric data set for the Amazon River channel (~ 1,100 km extension) using Brazilian nautical charts, and floodplain depths maps for high- and low-water periods of the flood wave in the middle-lower Amazon River

602 (average depth RMSE of 7.5 m and cross-sectional area error of 20.8%). We showed that our
603 approach using the distributed water level across the floodplain provides better topography
604 estimation than previous approaches. We also corrected the vegetation bias using ICESat-2
605 data, a recent and promising satellite for this application. Validation using locally derived
606 bathymetry showed an RMSE of 0.9 m for the floodplain bottom level. Topographic
607 floodplain mapping should be used with caution in the following regions: 1) areas where the
608 flood frequency is equal to or close to 100%; 2) areas distant from the Amazon River channel;
609 and 3) floodplain areas where the water level is very different from the river level, such as in
610 the low-period, when the water is blocked along the floodplain. Regarding the estimated high-
611 and low-water depth maps, we observed that the upstream to downstream trend in depths of
612 seasonally flooded areas agreeing with the findings of other studies. The variation of the
613 storage volume on the open-water floodplain is large (104.3 km^3) and varies on average each
614 year from 11.9 km^3 in low-water to 116.2 km^3 in the high-water period.
615 It should be noted that the SRTM3 DEM and MERIT DEM are topographic models
616 that do not represent topography in water bodies, and correcting this error is often not possible
617 because of the absence of bathymetric surveying. The approach presented here allowed the
618 topography estimation of these areas, i.e. temporarily flooded areas, without the need for
619 bathymetric surveying, but using water level data, and state-of-the-art of water cover mapping
620 (GSW database). In this way, the approach opens unprecedented opportunities for better
621 topographic representation in open water areas in any region of the globe, with the possibility
622 to use new altimetry data (such as ICESat-2 and SWOT) and imagery (such as Sentinel data).
623 Also, the flood frequency mapping can be performed using radar images that reduce the
624 systematic positive bias of vegetation due to the ability to penetrate the canopy (such as L-
625 band), allowing the estimation of bare-earth topography in seasonally flooded areas.
626 Furthermore, sediment deposition and erosion promote dynamic changes in surface

morphology in the fluvial channel and the floodplain. This evolution has been assessed using satellite images, but changes in the surface height are not usually estimated. Our method can be applied for different periods, for example, every 5 years, allowing the assessment of geomorphologic changes in a dynamic environment and quantification of the depositional and erosional history.

The datasets we developed can be used for different applications in hydrology, geomorphology, and ecology studies. Our analysis can help to assess the areas occupied by species that are limited by the water depth, such as aquatic macrophytes. Depth mapping in open water areas can also help map these species and estimate the carbon balance and primary productivity. Besides, topographic maps can provide insight into the floodplain geomorphology, the complex network of channels and the direction of channeled flows. Finally, it is expected that the elaborated database can be used in hydrodynamic simulations of the region, helping to understand water flows, inundated area patterns, and the water volume stored in the Amazon river-floodplain system.

Acknowledgments

Topographic and water depth maps of floodplain and Amazon River and the flood frequency map developed in this study are freely available at https://doi.org/10.17632/vn599y9szb.1. Supplementary data associated with this article can be found in the online version at xx. The authors would like to thank CNPq (Conselho Nacional de Desenvolvimento Científico e Tecnológico) for the doctoral fellowship granted to the first author (140352/2016-3) and CAPES (Coordenação de Aperfeiçoamento de Pessoal de Nível Superior) - Finance Code 001. They are grateful to Luna Alves and Daniel Moreira from CPRM (Companhia de Pesquisa de Recursos Minerais) for providing cross-sections of the Amazon River, and to Ayan Santos Fleischmann for the discussion and revision of the

manuscript. The authors would also like to thank two anonymous reviewers for their helpful comments. This study was carried out within the SWOT-MOD and SABERES projects. The project SABERES (Sustaining Amazon floodplain biodiversity and fisheries under climate change) is funded by the BNP Paribas foundation within its Climate & Biodiversity initiative 2019.

References

Alsdorf, D., Bates, P., Melack, J., Wilson, M., Dunne, T., 2007. Spatial and temporal complexity of the Amazon flood measured from space. Geophys. Res. Lett. 34, 1–5. https://doi.org/10.1029/2007GL029447

Alsdorf, D., Han, S.C., Bates, P., Melack, J., 2010. Seasonal water storage on the Amazon floodplain measured from satellites. Remote Sens. Environ. 114, 2448–2456. https://doi.org/10.1016/j.rse.2010.05.020

Alsdorf, D.E., Rodriguez, E., Lettenmaier, D.P., 2007. Measuring surface water from space. Rev. Geophys. 45, 1–24. https://doi.org/10.1029/2006RG000197.1.INTRODUCTION

Arsen, A., Crétaux, J.F., Berge-Nguyen, M., del Rio, R.A., 2013. Remote sensing-derived bathymetry of Lake Poopó. Remote Sens. 6, 407–420. https://doi.org/10.3390/rs6010407

Avisse, N., Tilmant, A., Müller, M.F., Zhang, H., 2017. Monitoring small reservoirs' storage with satellite remote sensing in inaccessible areas. Hydrol. Earth Syst. Sci. 21, 6445–6459.

Barbosa, C.C., 2005. Sensoriamento Remoto da dinâmica da circulaçnao da água do sistema planície de Curuai/ Rio Amazonas. Instituto de Pesquisas Espacia.

Barbosa, C.C.F., Novo, E.M.L. de M., Melack, J.M., Freitas, R.M. de, Pereira, W., 2006. A methodology for analysis of volume and flooded area dynamics: Lago Grande de Curuai várzea as an example. Rev. Bras. Cartogr. 58, 201–210.

Baugh, C.A., Bates, P.D., Schumann, G., Trigg, M.A., 2013. SRTM vegetation removal and hydrodynamic modeling accuracy. Water Resour. Res. 49, 5276–5289. https://doi.org/10.1002/wrcr.20412

679 Busker, T., De Roo, A., Gelati, E., Schwatke, C., Adamovic, M., Bisselink, B., Pekel, J.F., Cottam, A.,
680 2019. A global lake and reservoir volume analysis using a surface water dataset and satellite
681 altimetry. Hydrol. Earth Syst. Sci. 23, 669–690. https://doi.org/10.5194/hess-23-669-2019
682 Calmant, S., Da Silva, J.S., Moreira, D.M., Seyler, F., Shum, C.K., Crétaux, J.F., Gabalda, G., 2012.
683 Detection of Envisat RA2/ICE-1 retracked radar altimetry bias over the Amazon basin rivers
684 using GPS. Adv. Sp. Res. 51, 1551–1564. https://doi.org/10.1016/j.asr.2012.07.033
685 Castello, L., Isaac, V.J., Thapa, R., 2015. Flood pulse effects on multispecies fishery yields in the
686 Lower Amazon. R. Soc. Open Sci. https://doi.org/10.1098/rsos.150299
687 Chen, S., Michaelides, K., Grieve, S., Singer, M., 2019. Aridity is expressed in river topography
688 globally. Nature. https://doi.org/10.1038/s41586-019-1558-8
689 Danielson, J., Gesch, D., 2011. Global Multi-resolution Terrain Elevation Data 2010(GMTED2010).
690 U.S. Geol. Surv. Open-File Rep. 2011–1073 2010, 26. https://doi.org/citeulike-article-
691 id:13365221
692 Dunne, T., Mertes, L.A.K., Meade, R.H., Richey, J.E., Forsberg, B.R., 1998. Exchanges of sediment
693 between the flood plain and chennel of the Amazon River in Brazil. Geol. Soc. Am. Bull. 110,
694 450–467. https://doi.org/10.1130/0016-7606(1998)110<0450
695 Farr, T., Rosen, P., Caro, E., Crippen, R., Duren, R., Hensley, S., Kobrick, M., Paller, M., Rodriguez,
696 E., Roth, L., Seal, D., Shaffer, S., Shimada, J., Umland, J., Werner, M., Oskin, M., Burbank, D.,
697 Alsdorf, D., 2007. The shuttle radar topography mission. Rev. Geophys. 45, 1–33.
698 https://doi.org/10.1029/2005RG000183
699 Fassoni-Andrade, A.C., Paiva, R.C.D. de, 2019. Mapping spatial-temporal sediment dynamics of
700 river-floodplains in the Amazon. Remote Sens. Environ. 221, 94–107.
701 https://doi.org/10.1016/j.rse.2018.10.038
702 Fassoni-Andrade, A.C., Paiva, R.C.D., Fleischmann, A.S., 2020. Lake topography and active storage
703 from satellite observations of flood frequency. Water Resour. Res. 56.
704 https://doi.org/10.1029/2019wr026362
705 Feng, L., Hu, C., Chen, X., Li, R., Tian, L., Murch, B., 2011. MODIS observations of the bottom
706 topography and its inter-annual variability of Poyang Lake. Remote Sens. Environ. 115, 2729–

2741. https://doi.org/10.1016/j.rse.2011.06.013

Filizola, N., Latrubesse, E.M., Fraizy, P., Souza, R., Guimarães, V., Guyot, J.L., 2014. Was the 2009 flood the most hazardous or the largest ever recorded in the Amazon? Geomorphology 215, 99–105. https://doi.org/10.1016/j.geomorph.2013.05.028

Frappart, F., Papa, F., Güntner, A., Tomasella, J., Pfeffer, J., Ramillien, G., Emilio, T., Schietti, J., Seoane, L., da Silva Carvalho, J., Medeiros Moreira, D., Bonnet, M.P., Seyler, F., 2019. The spatio-temporal variability of groundwater storage in the Amazon River Basin. Adv. Water Resour. 124, 41–52. https://doi.org/10.1016/j.advwatres.2018.12.005

Getirana, A., Chul, H., Tseng, K., 2018. Deriving three dimensional reservoir bathymetry from multi-satellite datasets. Remote Sens. Environ. 217, 366–374. https://doi.org/10.1016/j.rse.2018.08.030

Gorelick, N., Hancher, M., Dixon, M., Ilyushchenko, S., Thau, D., Moore, R., 2017. Google Earth Engine: Planetary-scale geospatial analysis for everyone. Remote Sens. Environ. 202, 18–27. https://doi.org/10.1016/j.rse.2017.06.031

Hamilton, S.K., Sippel, S.J., Melack, J.M., 2004. Seasonal inundation patterns in two large savanna floodplains of South America: The Llanos de Moxos (Bolivia) and the Llanos del Orinoco (Venezuela and Colombia). Hydrol. Process. 18, 2103–2116. https://doi.org/10.1002/hyp.5559

Hess, L.L., Melack, J.M., Affonso, A.G., Barbosa, C., Gastil-Buhl, M., Novo, E.M.L.M., 2015. Wetlands of the Lowland Amazon Basin: Extent, Vegetative Cover, and Dual-season Inundated Area as Mapped with JERS-1 Synthetic Aperture Radar. Wetlands 35, 745–756. https://doi.org/10.1007/s13157-015-0666-y

Hutchinson, M.F., 1989. A new procedure for gridding elevation and stream line data with automatic removal of spurious pits. J. Hydrol. 106, 211–232. https://doi.org/10.1016/0022-1694(89)90073-5

Ji, X., Lesack, L.F.W., Melack, J.M., Wang, S., Riley, W.J., Shen, C., 2019. Seasonal and inter-annual patterns and controls of hydrological fluxes in an Amazon floodplain lake with a surface-subsurface processes model. Water Resour. Res. 55, 3056–3075. https://doi.org/10.1029/2018WR023897

Junk, W., Bayley, P.B., Sparks, R.E., 1989. The flood pulse concept in river-floodplain-systems. Can.

735 J. Fish. Aquat. Sci. 106, 110–127. https://doi.org/10.1371/journal.pone.0028909
736 Junk, W.J., Piedade, M.T.F., 1997. Plant Life in the Floodplain with Special Reference to Herbaceous
737 Plants, in: The Central Amazon Floodplain. Springer, Berlin, pp. 147–185.
738 https://doi.org/10.1007/978-3-662-03416-3_8
739 Junk, W.J., Piedade, M.T.F., Schöngart, J., Cohn-Haft, M., Adeney, J.M., Wittmann, F., 2011. A
740 classification of major naturally-occurring amazonian lowland wetlands. Wetlands 31, 623–640.
741 https://doi.org/10.1007/s13157-011-0190-7
742 Junk, W.J., Piedade, M.T.F., Schöngart, J., Wittmann, F., 2012. A classification of major natural
743 habitats of Amazonian white-water river floodplains (várzeas). Wetl. Ecol. Manag. 20, 461–475.
744 https://doi.org/10.1007/s11273-012-9268-0
745 Kosuth, P., Callede, J., Laraque, A., Filizola, N., Guyot, J.L., Seyler, P., Fritsch, J.M., Guimarães, V.,
746 2009. Sea-tide effects on flows in the lower reaches of the Amazon River. Hydrol. Process. 23,
747 3141–3150. https://doi.org/10.1002/hyp.7387
748 Krieger, G., Moreira, A., Fiedler, H., Hajnsek, I., Werner, M., Younis, M., Zink, M., 2007. TanDEM-
749 X: A satellite formation for high-resolution SAR interferometry, in: IEEE Transactions on
750 Geoscience and Remote Sensing. pp. 3317–3340. https://doi.org/10.1109/TGRS.2007.900693
751 Latrubesse, E.M., 2012. Amazon lakes, in: Bengtsson, L., Herschy, R.W., Fairbridge, R.W. (Eds.),
752 Encyclopedia of Lakes and Reservoirs. Springer Verlag, pp. 13–26. https://doi.org/10.1007/978-
753 1-4020-4410-6
754 Latrubesse, E.M., Franzinelli, E., 2002. The Holocene alluvial plain of the middle Amazon River,
755 Brazil. Geomorphology 44, 241–257. https://doi.org/10.1016/S0169-555X(01)00177-5
756 Lesack, F.W., Melack, J.M., 1995. Flooding hydrology and mixture dynamics of lakewater derived
757 from multiple sources in an Amazon floodplain lake. Water Resour. Res. 31, 329–345.
758 Loughlin, F.E.O., Paiva, R.C.D., Durand, M., Alsdorf, D.E., Bates, P.D., 2016. Remote Sensing of
759 Environment A multi-sensor approach towards a global vegetation corrected SRTM DEM
760 product. Remote Sens. Environ. 182, 49–59. https://doi.org/10.1016/j.rse.2016.04.018
761 Martins, V.S., Novo, E.M.L.M., Lyapustin, A., Aragão, L.E.O.C., Freitas, S.R., Barbosa, C.C.F.,
762 2018. Seasonal and interannual assessment of cloud cover and atmospheric constituents across

763 the Amazon (2000–2015): Insights for remote sensing and climate analysis. ISPRS J.
764 Photogramm. Remote Sens. 0–1. https://doi.org/10.1016/j.isprsjprs.2018.05.013
765 Melack, J.M., Novo, E.M.L.M., Forsberg, B.R., Piedade, M.T.F., Maurice, L., 2009. Floodplain
766 Ecosystem Processes, in: Amazonia and Global Change. https://doi.org/10.1029/2008GM000727
767 Mertes, L. a K., Dunne, T., Martinelli, L. a., 1996. Channel-floodplain geomorphology along the
768 Solimoes-Amazon River, Brazil. Bull. Geol. Soc. Am. 108, 1089–1107.
769 https://doi.org/10.1130/0016-7606(1996)108<1089:CFGATS>2.3.CO;2
770 Messager, M.L., Lehner, B., Grill, G., Nedeva, I., Schmitt, O., 2016. Estimating the volume and age of
771 water stored in global lakes using a geo-statistical approach. Nat. Commun. 1–11.
772 https://doi.org/10.1038/ncomms13603
773 Moreira, D.M., 2016. Geodésia Aplicada ao Monitoramento Hidrológico da Bacia Amazônica.
774 Universidade Federal do Rio de Janeiro. https://doi.org/10.1017/CBO9781107415324.004
775 O'Loughlin, F.E., Neal, J., Yamazaki, D., Bates, P.D., 2016. ICESat-derived inland water surface spot
776 heights. Water Resour. Res. 52, 3276–3284. https://doi.org/10.1002/2015WR018237
777 Paiva, R.C.D. de, Buarque, D.C., Collischonn, W., Bonnet, M.P., Frappart, F., Calmant, S., Bulhões
778 Mendes, C.A., 2013. Large-scale hydrologic and hydrodynamic modeling of the Amazon River
779 basin. Water Resour. Res. 49, 1226–1243. https://doi.org/10.1002/wrcr.20067
780 Park, E., Latrubesse, E.M., 2017. The hydro-geomorphologic complexity of the lower Amazon River
781 floodplain and hydrological connectivity assessed by remote sensing and field control. Remote
782 Sens. Environ. 198, 321–332. https://doi.org/10.1016/j.rse.2017.06.021
783 Pekel, J.-F., Cottam, A., Gorelick, N., Belward, A.S., 2016. High-resolution mapping of global surface
784 water and its long-term changes. Nature 540, 418–422. https://doi.org/10.1038/nature20584
785 Piedade, M.T.F., 1993. Biologia e Ecologia de Echinochloa poystachya (H.B.K.) Hitchcock
786 (Gramineae = Poaeceae), Capim Semi-Aquático da Várzea Amazonica. Acta Limnológica Bras.
787 6, 173–185.
788 Pinel, S.S.L., 2017. Amazonian floodplain hydrodynamics: Characterization and local modeling with
789 in situ and remotely sensed data. Universidade do estado do Amazonas.
790 Rodríguez, E., Morris, C.S., Belz, J.E., 2006. A Global Assessment of the SRTM Performance 72,

249–260.

Rudorff, C.M., Melack, J.M., Bates, P.D., 2014a. Flooding dynamics on the lower Amazon floodplain: 1. Hydraulic controls on water elevation, inundation extent, and river-floodplain discharge. Water Resour. Res. 50, 619–634. https://doi.org/10.1002/2013WR014091

Rudorff, C.M., Melack, J.M., Bates, P.D., 2014b. Flooding dynamics on the lower Amazon floodplain: 2. Seasonal and interannual hydrological variability. Water Resour. Res. 50, 635–649. https://doi.org/10.1002/2013WR014714

Silva, T.S.F., Costa, M.P.F., Melack, J.M., 2010. Spatial and temporal variability of macrophyte cover and productivity in the eastern Amazon floodplain: A remote sensing approach. Remote Sens. Environ. 114, 1998–2010. https://doi.org/10.1016/j.rse.2010.04.007

Silva, T.S.F., Melack, J.M., Novo, E.M.L.M., 2013. Responses of aquatic macrophyte cover and productivity to flooding variability on the Amazon floodplain. Glob. Chang. Biol. 19, 3379–3389. https://doi.org/10.1111/gcb.12308

Sippel, S.J., Hamilton, S.K., Melack, J.M., 1992. Inundation Area and Morphometry of Lakes on the Amazon River Floodplain, Brazil. Arch. Fur Hydrobiol. 123, 385–400.

Tachikawa, T., Kaku, M., Iwasaki, A., Gesch, D., Oimoen, M., Zhang, Z., Danielson, J., Krieger, T., Curis, B., Haase, J., Abrams, M., Crippen, R., Carabajal, C., 2011. ASTER Global Digital Elevation Model Version 2 – Summary of Validation Results, ASTER GDEM Validation Team. https://doi.org/10.1017/CBO9781107415324.004

Trigg, M.A., Bates, P.D., Wilson, M.D., Schumann, G., Baugh, C., 2012. Floodplain channel morphology and networks of the middle Amazon River. Water Resour. Res. 48, 1–17. https://doi.org/10.1029/2012WR011888

Trigg, M.A., Wilson, M.D., Bates, P.D., Horritt, M.S., Alsdorf, D.E., Forsberg, B.R., Vega, M.C., 2009. Amazon flood wave hydraulics. J. Hydrol. 374, 92–105. https://doi.org/10.1016/j.jhydrol.2009.06.004

Tseng, K.H., Kuo, C.Y., Lin, T.H., Huang, Z.C., Lin, Y.C., Liao, W.H., Chen, C.F., 2017. Reconstruction of time-varying tidal flat topography using optical remote sensing imageries. ISPRS J. Photogramm. Remote Sens. 131, 92–103.

https://doi.org/10.1016/j.isprsjprs.2017.07.008

Tseng, K.H., Shum, C.K., Kim, J.W., Wang, X., Zhu, K., Cheng, X., 2016. Integrating Landsat Imageries and Digital Elevation Models to Infer Water Level Change in Hoover Dam. IEEE J. Sel. Top. Appl. Earth Obs. Remote Sens. 9, 1696–1709. https://doi.org/10.1109/JSTARS.2015.2500599

Urban, T.J., Schutz, B.E., Neuenschwander, A.L., 2008. A survey of ICESat coastal altimetry applications: Continental Coast, Open Ocean Island, and Inland River, in: Terrestrial, Atmospheric and Oceanic Sciences. pp. 1–19. https://doi.org/10.3319/TAO.2008.19.1-2.1(SA)

Wilson, M.D., Bates, P., Alsdorf, D., Forsberg, B., Horritt, M., Melack, J., Frappart, F., Famiglietti, J., 2007. Modeling large-scale inundation of Amazonian seasonally flooded wetlands. Geophys. Res. Lett. 34, 4–9. https://doi.org/10.1029/2007GL030156

Yamazaki, D., Baugh, C.A., Bates, P.D., Kanae, S., Alsdorf, D.E., Oki, T., 2012. Adjustment of a spaceborne DEM for use in floodplain hydrodynamic modeling. J. Hydrol. 436–437, 81–91. https://doi.org/10.1016/j.jhydrol.2012.02.045

Yamazaki, D., Ikeshima, D., Tawatari, R., Yamaguchi, T., O'Loughlin, F., Neal, J.C., Sampson, C.C., Kanae, S., Bates, P.D., 2017. A high-accuracy map of global terrain elevations. Geophys. Res. Lett. 44, 5844–5853. https://doi.org/10.1002/2017GL072874

Zwally, H. J., R. Schutz, C. Bentley, J. Bufton, T. Herring, J. Minster, J. Spinhirne, and R. Thomas. 2014. *GLAS/ICESat L2 Global Land Surface Altimetry Data, Version 34*. Boulder, Colorado USA. NASA National Snow and Ice Data Center Distributed Active Archive Center. doi: https://doi.org/10.5067/ICESAT/GLAS/DATA227.

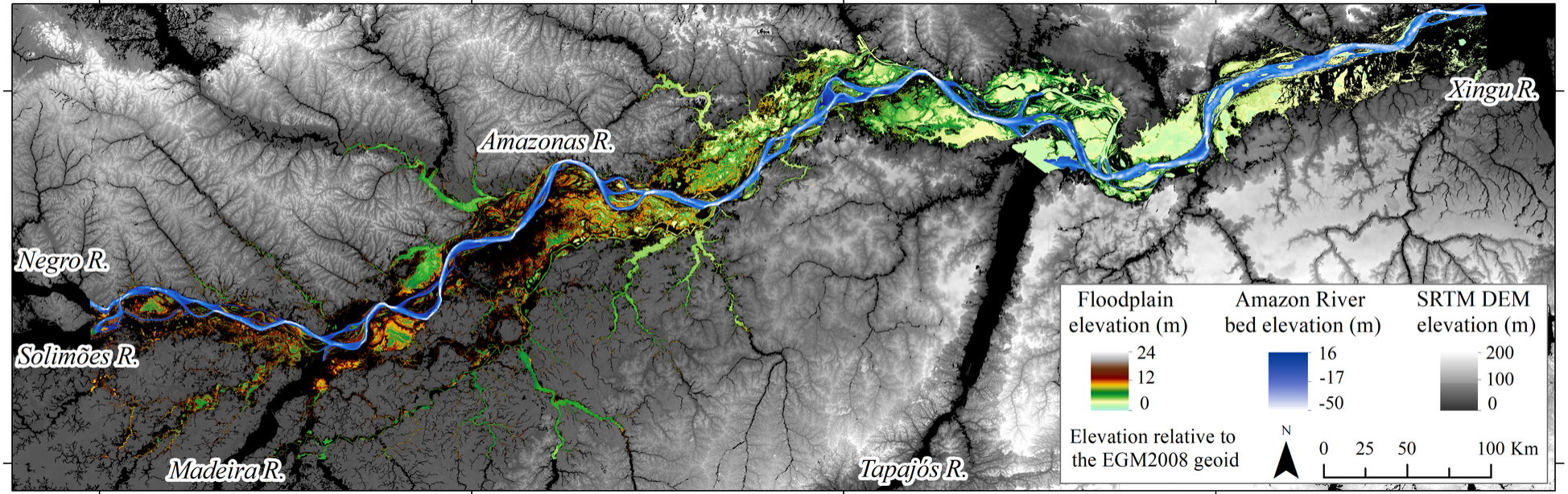
60° W
58° W
56° W
54° W
2° S
4° S
Amazonas R.
Xingu R.
Negro R.
Solimões R.
Madeira R.
Tapajós R.
Floodplain elevation (m)
24
12
0
Amazon River bed elevation (m)
16
-17
-50
SRTM DEM elevation (m)
200
100
0
Elevation relative to the EGM2008 geoid
N
0 25 50 100 Km